# Ligand Lipophilicity Determines Molecular Mechanisms of

# Nanoparticle Adsorption to Lipid Bilayers

Carlos A. Huang-Zhu $^{l\dagger}$ , Jonathan K. Sheavly $^{l\dagger}$ , Alex K. Chew $^{l}$ , Samarthaben J. Patel $^{l}$ , and Reid C. Van Lehn $^{l,2}*$ 

#### **ABSTRACT**

The interactions of ligand-functionalized nanoparticles with the cell membrane affect cellular uptake, cytotoxicity, and related behaviors, but relating these interactions to ligand properties remains challenging. In this work, we perform coarse-grained molecular dynamics simulations to study how the adsorption of ligandfunctionalized cationic gold nanoparticles (NPs) to a single-component lipid bilayer (as a model cell membrane) is influenced by ligand end group lipophilicity. A set of 2-nm diameter NPs, each coated with a monolayer of organic ligands that differ only in their end groups, was simulated to mimic NPs recently studied experimentally. Metadynamics calculations were performed to determine key features of the free energy landscape for adsorption as a function of the distance of the NP from the bilayer and the number of NP-lipid contacts. These simulations revealed that NP adsorption is thermodynamically favorable for all NPs due to the extraction of lipids from the bilayer and into the NP monolayer. To resolve ligand-dependent differences in adsorption behavior, string method calculations were performed to compute minimum free energy pathways for adsorption. These calculations revealed a surprising non-monotonic dependence of the free energy barrier for adsorption on ligand end group lipophilicity. Large free energy barriers are predicted for the least lipophilic end groups because favorable NPlipid contacts are initiated only through the unfavorable protrusion of lipid tail groups out of the bilayer. The smallest free energy barriers are predicted for end groups of intermediate lipophilicity which promote NP-lipid contacts by intercalating within the bilayer. Unexpectedly, large free energy barriers are also predicted for the most lipophilic end groups which remain sequestered within the ligand monolayer rather than intercalating within the bilayer. These trends are broadly in agreement with past experimental measurements and reveal how subtle variations in ligand lipophilicity dictate adsorption mechanisms and associated kinetics by influencing the interplay of lipid-ligand interactions.

KEYWORDS: nanoparticles, lipid bilayer, adsorption, molecular dynamics, coarse-grained simulations

<sup>&</sup>lt;sup>1</sup>Department of Chemical and Biological Engineering, University of Wisconsin – Madison, Madison, WI, 53706, United States.

<sup>&</sup>lt;sup>2</sup>Department of Chemistry, University of Wisconsin – Madison, Madison, WI, 53706, United States.

<sup>†</sup>these authors equally contributed to the manuscript

<sup>\*</sup>send correspondence to: <u>vanlehn@wisc.edu</u>

#### INTRODUCTION

Ligand-functionalized gold nanoparticles (NPs) provide platforms for a wide variety of biomedical applications, including drug delivery, biosensing, and photothermal therapy. 1-5 These applications are facilitated by grafting a self-assembled monolayer of organic ligands to the NP surface to modulate interactions with biological materials. 6-10 Selecting or designing ligands to mediate desired nano-bio interactions is a central challenge – and opportunity - for NP applications. Ligands are commonly designed using a modular structure comprising separately selected backbone and end group moieties. 11-13 Ligand backbones are often alkane chains of varying length, possibly with an ethylene glycol segment inserted to confer stability in biological environments, <sup>14</sup> while end groups can include a wide variety of moieties of varying charge, size, and lipophilicity (i.e., thermodynamic affinity for lipids).<sup>6–10</sup> Varying the ligand backbone and end group properties, as well as the relative proportions of different ligands in multicomponent ligand monolayers, 15 thus leads to a large feasible design space of NP compositions. To guide ligand design, experimental studies have systematically investigated how variations to ligand properties such as end group charge or lipophilicity affect behaviors including cellular uptake, 16,17 cytotoxicity, 16,18,19 antimicrobial activity, 20,21 and immunological response. 22,23 Recent computational models have also related descriptors of NP properties to experimentally measured biological activities. 24-31 However, predicting how ligand structure influences nano-bio interactions remains challenging because subtle differences in ligand chemical properties can manifest as large changes in NP behavior (e.g., swapping the positions of charged moieties in zwitterionic end groups can substantially influence cellular uptake<sup>17</sup>). This challenge is exacerbated for small (<10 nm in diameter) NPs because the free volume accessible to ligands in the monolayer can influence ligand conformations, which has motivated a number of molecular simulation studies to understand how the interplay of NP size and ligand properties affects the surface properties of NPs in solution. 31-40

Understanding how ligand properties influence interactions between NPs and cell membranes is of particular biomedical importance. <sup>9,41–43</sup> For example, NP adsorption to the cell membrane can drive intracellular transport, <sup>44</sup> which is critical for applications requiring delivery of NPs to the cell interior, but may also cause membrane disruption and cytotoxicity. <sup>45,46</sup> Given the complex composition of the cell membrane, simplified lipid bilayer systems, such as supported lipid bilayers (SLBs) and lipid vesicles with a small number of components, are routinely used experimentally as model membranes to enable mechanistic studies of NP-bilayer interactions. <sup>47</sup> Experimental studies of NP-bilayer interactions can be related to biologically relevant behaviors; for example, the adsorption of NPs to lipid bilayers correlates with endocytic uptake, <sup>44</sup> NP-induced disruption of lipid bilayers correlates with cytotoxicity, <sup>48</sup> and the insertion of amphiphilic NPs into lipid bilayers correlates with nonendocytic cell entry. <sup>49</sup> The simplicity of these model systems further permits comparisons to molecular dynamics (MD) simulations. For example, all-atom (AA) and coarse-grained (CG) MD simulations have revealed pathways by which amphiphilic NPs insert into lipid bilayers, <sup>50–54</sup> explained the preferential adsorption of NPs to different lipid phases or phase boundaries, <sup>55–58</sup> and explored the effect of NP charge on bilayer adsorption. <sup>59–62</sup> Together, experiments and corresponding simulations with model membranes permit analysis of how ligand properties affect nano-bio interactions.

Recently, we combined experiments and AA MD simulations to explore the relationship between the lipophilicity of ligand end groups and NP adsorption to single-component lipid bilayers.<sup>63</sup> We studied a library of gold NPs with 2 nm core diameters, each protected by a monolayer of ligands with the structure shown in Figure 1A. Each ligand was composed of (1) a backbone consisting of a lipophilic alkanethiol segment and hydrophilic tetraethylene(glycol) segment and (2) an R group consisting of a cationic quaternary ammonium group substituted with two methyl groups and an R group. Different R groups were selected to vary their lipophilicity and the adsorption of the resulting NPs on a 1,2-dioleoyl-sn-glycero-3-phosphocholine (DOPC) SLB was measured via quartz crystal microbalance with dissipation (QCM-D) experiments.<sup>63</sup> These experiments found that increased R group lipophilicity resulted in increased adsorbed mass and increased rate of adsorption as measured by QCM-D. Notably, only the most lipophilic R groups (C<sub>9</sub> and C<sub>1</sub>Bn in Figure 1B) remained adsorbed after extended rinsing, indicating irreversible adsorption to the SLB. AA MD simulations, coupled with umbrella sampling calculations,

were used to compute the potential of mean force (PMF) for NP adsorption to explain this behavior. PMFs computed by using the distance between the NP and the bilayer center as a collective variable (CV) revealed that adsorption is thermodynamically favorable once sufficient contacts between lipophilic ligand R groups and lipid tails are formed. Separate PMF calculations using the number of these hydrophobic contacts as a CV indicated that contacts were promoted by ligands intercalating within the bilayer, suggesting that intercalation promotes irreversible adsorption. However, the computational expense of AA MD simulations limited these studies to sampling only a single CV at a time for a limited number of NPs, inhibiting more detailed analysis of the impact of ligand R group properties on mechanisms of adsorption and limiting the number of ligand R groups that could be studied.

In this work, we perform CG MD simulations to further investigate the thermodynamics and associated mechanisms of NP adsorption to single-component lipid bilayers as a function of ligand R group lipophilicity. We perform metadynamics calculations to compute the free energy landscape for NP adsorption using both the distance of the NP from the bilayer and the number of NP-lipid contacts as CVs, revealing local free energy minima associated with (1) the adsorption of the NP onto the bilayer and (2) the extraction of lipids from the bilayer and into the ligand monolayer. To further resolve ligand-dependent adsorption mechanisms, we use the string method with swarms of trajectories<sup>64-67</sup> to compute minimum energy paths (MFEPs) for NP adsorption to the upper leaflet of the bilayer from an initial state in solution. The MFEP is defined as the path with the highest likelihood of NP adsorption and is used to quantify the free energy barrier that each NP must cross to adsorb to the bilayer. Comparing the free energy barrier for adsorption for seven different NPs reveals an unexpected nonmonotonic dependence on R group lipophilicity. All seven NPs demonstrate deep minima associated with adsorption without a clear trend in the global adsorption free energy minimum. We relate these findings to the likelihood of lipids to extract from the bilayer and the competition between the intercalation of lipophilic ligands within the bilayer or within the hydrophobic core of the ligand monolayer. Together, these results provide mechanistic insights into kinetic phenomena underlying NP adsorption and how they depend non-intuitively on ligand R group properties.

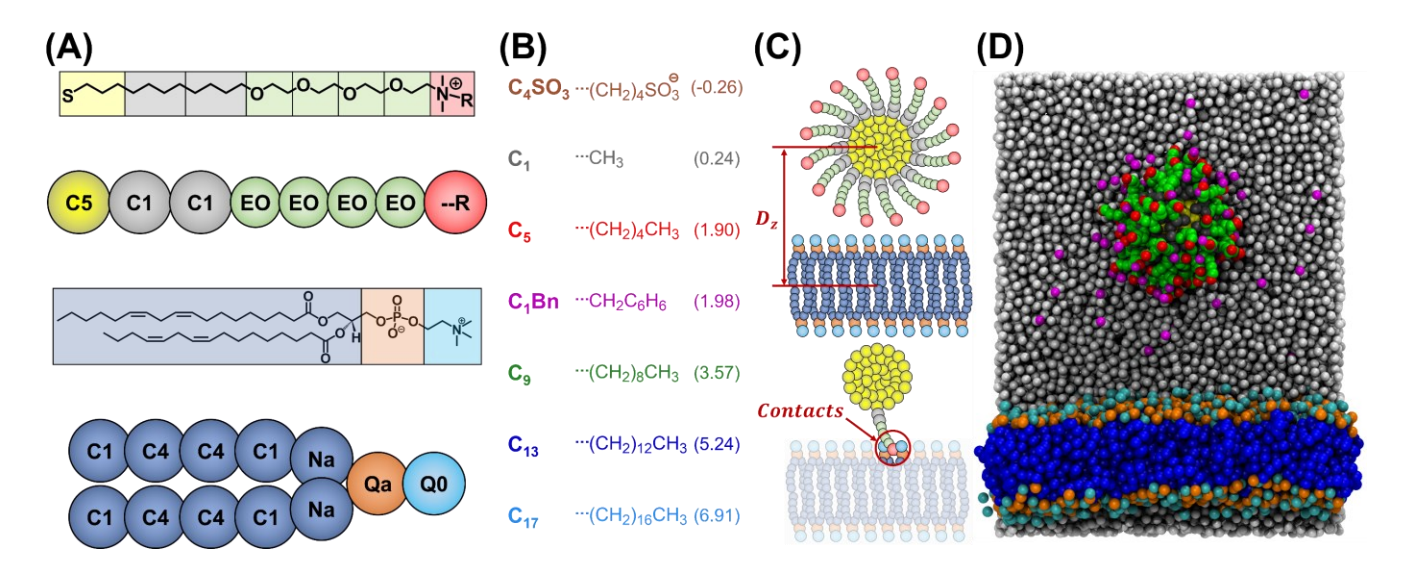


**Figure 1**. (A) AA and CG representations of the ligand chemical structure and the DIPC lipid. Chemical groups are colored according to their coarse-grained bead. (B) Seven R groups studied with their corresponding chemical structure and LogP values. Label colors are consistent with colors used in other figures. (C) Schematic illustrating the defined CVs. For each lipid, the choline group is colored cyan, the phosphate group is colored orange, and the tails are colored blue. Water molecules and counterions are included in all simulations but are excluded from this schematic. (D) Snapshot of an equilibrated simulation of a C<sub>1</sub> NP solvated in water (white) neutralized with

Cl<sup>-</sup> counterions (magenta) and far from a DIPC bilayer; color scheme follows (A). Visual Molecular Dynamics (VMD)<sup>68</sup> was used to generate all simulation snapshots.

#### RESULTS AND DISCUSSION

Free energy landscape reveals NP adsorption and desorption modulated by lipid extraction.

In our past computational and experimental study, we found that the adsorption of NPs (functionalized with a subset of the ligands shown in Figure 1B) to DOPC lipid bilayers depends upon the lipophilicity of the ligand R group. 63 Increasing R group lipophilicity led to a transition from a reversibly adsorbed state to an irreversibly adsorbed state as quantified using QCM-D experimental measurements. AA simulations indicated that this difference could be related to the propensity of more lipophilic ligands to intercalate within the bilayer, eventually leading to the extraction of lipids from the bilayer and into the ligand monolayer. 63 However, it is too computationally expensive to sample the free energy landscape underlying the extraction of lipids using AA simulations, motivating CG simulations to model the adsorption process for a larger set of ligand R groups in this study to understand mechanisms influencing NP adsorption as a function of ligand properties. Figure 1A shows the chemical structures and CG models of the cationic ligand structure and DIPC lipid (which has 16-18 carbon tails with two cis-unsaturated bonds on each tail and is used to represent DOPC in the CG simulations), and Figure 1B shows the seven ligand R groups we used in this study. Each R group is labeled with a corresponding value of its octanol-water partition coefficient (LogP) as a measure of lipophilicity; larger, more positive values of LogP indicate increasingly lipophilic R groups. The seven R groups span a range of LogP values and consist of five R groups with varying alkyl chain lengths (C<sub>1</sub>, C<sub>5</sub>, C<sub>9</sub>, C<sub>13</sub>, and C<sub>17</sub>), a benzyl group (C<sub>1</sub>Bn), and an alkyl chain terminated in a sulfonate group (C<sub>4</sub>SO<sub>3</sub>). Ligands with all R groups excluding C<sub>4</sub>SO<sub>3</sub> have a net positive charge due to the quaternary ammonium groups; the negative charge on the C<sub>4</sub>SO<sub>3</sub> group causes its corresponding ligand to be neutral. This set of ligand exceeds those that we previously studied<sup>63</sup> by including longer alkyl groups (C<sub>13</sub> and C<sub>17</sub>) to probe larger values of LogP and by including the zwitterionic C<sub>4</sub>SO<sub>3</sub> to probe the impact of R group charge. CG parameters for all ligands were obtained following a bottom-up approach by reproducing more accurate AA MD simulations as detailed in the SI (Figure S6-S11).

To first gain insight into NP-bilayer adsorption behavior, we performed 2D well-tempered metadynamics simulations in a space defined by two collective variables (CVs): the distance between the NP and the bilayer ( $D_z$ ) and the number of contacts formed between the NP and the bilayer (contacts). A representative schematic of these CVs is shown in Figure 1C. Four walkers were simultaneously sampled every 400 ps during 500 ns production runs for a total of 2  $\mu$ s of sampling time. Figure 2 shows the free energy landscape for the adsorption of the C<sub>1</sub> NP to a DIPC lipid bilayer. An upper wall is imposed to restrict the NP to sample values of  $D_z$  close to the bilayer (described in the Methods section) which may bias the numerical values of the free energies obtained from these calculations. Nonetheless, the metadynamics calculations are valuable for qualitatively identifying several important regions in the free energy landscape for NP adsorption; Figure 2 labels important regions with points and shows corresponding simulation snapshots. We now describe these points sequentially to highlight the sequence of events that may occur during the interaction with a bilayer.

The initial configuration of the NP is point A, which corresponds to a NP in solution away from the bilayer (large  $D_z$ ) and not in contact with any lipids (zero contacts). The free energy in this region is a local minimum. The NP can then approach the bilayer (decreasing value of  $D_z$ ), which is associated with an increase in free energy, until reaching point B. Point B corresponds to the free energy barrier for adsorption and occurs when the NP initiates contacts with the bilayer. Metadynamics simulations do not sample the free energy landscape with sufficiently fine resolution near the free energy barrier to resolve its value; this limitation, as well as the limitation associated with the upper wall noted above, motivates the use of the string method with swarms of trajectories and umbrella sampling to compute this barrier (*vide infra*). Further decreasing  $D_z$  from point B likewise increases the number of contacts to reach point C, which lies within a low free energy basin. The snapshot at this point illustrates that

the increase in contacts is due to the extraction of lipids from the bilayer and into the ligand monolayer. Once sufficient lipids are extracted, the NP adsorbs to the upper leaflet and the bilayer relaxes the deformations associated with the adsorption process, leading to a local free energy minimum at point D. Taken together, analysis of the free energy landscape indicates that NP adsorption is favorable due to lipid extraction that occurs after the NP initiates favorable contact with the hydrophobic core of the bilayer, which is in agreement with our prior AA MD simulations. Further analysis confirming that lipid extraction is thermodynamically favorable, in agreement with this result, is presented in the SI (Figures S1-S5).

The sequence represented by points A-D represents the expected adsorption process and highlights the importance of lipid extraction from the bilayer to stabilize the adsorbed state. However, the metadynamics calculations further reveal that the free energy landscape includes a region associated with the desorption of a NP with extracted lipids. Specifically, increasing  $D_z$  from point D with the number of contacts approximately constant leads to point E, in which the NP begins to detach from the bilayer while maintaining a "lipid bridge." The bridge eventually relaxes when the NP completely desorbs into solution at point F. Point F is similar to point A, but is lower in free energy due to the favorable extraction of lipids from the bilayer; extracted lipids fill free volume within the NP monolayer to shield hydrophobic NP surface area from water in agreement with prior simulations.<sup>37,51,63</sup> There is no apparent pathway from point A to point F without passing through a surface-adsorbed state; therefore, free energy calculations that sample only  $D_z$  as a CV may fail to detect point F which could lead to a bias in free energy calculations depending upon the manner in which initial configurations are generated (e.g., by permitting the extraction of lipids or not). 50,63 Indeed, this behavior was observed in our past AA MD simulations, in which we observed hysteresis in the free energy computed as a function of  $D_z$  depending on whether initial configurations included large numbers of lipid contacts. 63 The results and configurations obtained in Figure 2 are thus consistent with those AA simulations and indicate that favorable lipid extraction occurs over long timescales not sampled in the AA simulations, highlighting the importance of explicitly biasing the formation of NP-bilayer contacts.

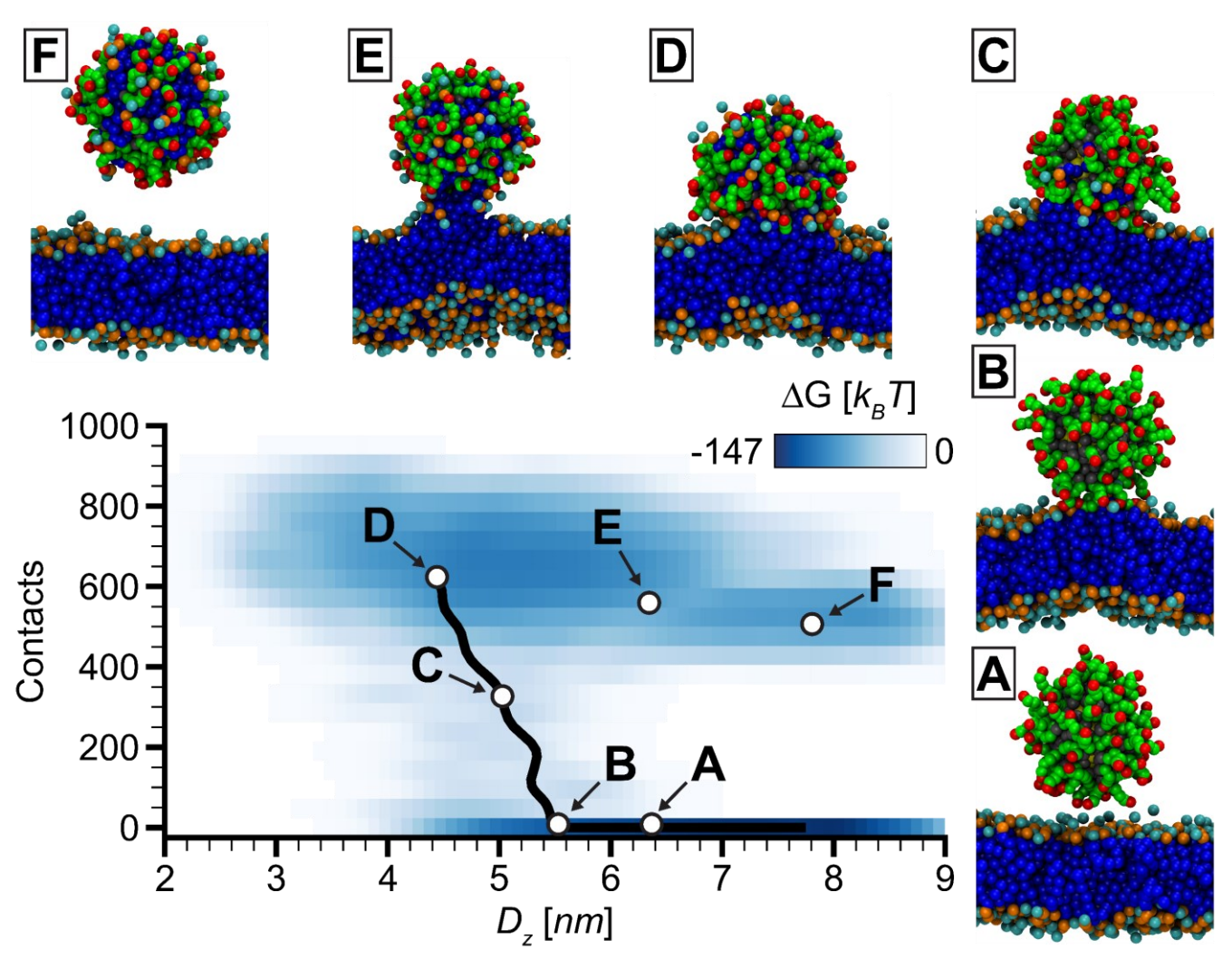


**Figure 2.** Free energy landscape for the adsorption of the  $C_1$  NP computed using metadynamics. Regions of the free energy landscape are labeled according to representative simulation snapshots that show the NP-bilayer interactions at the defined set of CVs. Note that an upper wall is imposed to prevent large values of  $D_z$  from being sampled (as described in the Methods). The MFEP computed using the string method with swarms of trajectories is overlaid (black line) to show that the MFEP connects two low free energy basins on the landscape. In the simulation snapshots, the NP and lipids are color coded as described in Figure 1A. Water molecules and ions are not shown. Lipids from the bilayer that are in front of the center of mass of the NP and farther than 2.5 nm of the S1 beads are not shown to visualize ligand intercalation in the bilayer while allowing visualization of lipids extracted onto the NP monolayer.

# Potentials of mean force along the minimum free energy paths for NP adsorption

To complement the mechanistic insight gained from resolving the free energy landscape, and to more accurately resolve the free energy barrier for NP adsorption, we established an alternative approach to compute a potential of mean force (PMF) using 1D umbrella sampling. We computed the most probable path for NP adsorption to the bilayer in terms of the same two CVs used during metadynamics by using the string method with swarms of trajectories, as described in the Methods section and schematically illustrated in Figure S13, to compute the MFEP. <sup>64–67</sup> This approach involves iteratively evolving strings composed of sets of physically relevant CV values toward a converged path between two free energy basins, labeled by states A and D in Figure 2, that passes through state C. The converged path is defined as the MFEP. To confirm the validity of the MFEP calculations, Figure 2 overlays the final converged string for one replica of the C<sub>1</sub> NP on the free energy landscape to show

that it samples CV regions associated with an increase in NP-bilayer contacts and a decrease in  $D_z$ . The evolution of strings for all seven NPs (one replica) are included in the SI (Figures S14-S20); MFEPs for all seven NPs appear similar to the MFEP shown in Figure 2. The MFEP was expressed using path CV equations<sup>67</sup> described by the distance along the path, S, and the distance away from the path, S. 1D PMFs were then computed as a function of S, with additional details and data on convergence described in the SI (Figure S21-S26).

Figure 3A shows PMFs as a function of S for all seven NPs. All PMFs have qualitatively similar features; PMFs for additional replicas are shown in the SI (Figure S27-S33) and exhibit similar features. Low values of S correspond to configurations where the NP is in solution far from the bilayer (state A in Figure 2 with large  $D_z$  and zero contacts). Accordingly, PMF values were set to zero for S=0 so that the PMF represents the change in free energy associated with NP adsorption from an initial state in solution. All PMFs exhibit maxima for 0.3 < S < 0.5. These values of S correspond to state B in Figure 2 where the NP comes close to the bilayer and initiates contact with the lipids, followed by lipid extraction after enough contacts are made. We associate these PMF maxima with NP-specific free energy barriers for adsorption, as discussed in detail below. Some PMFs also exhibit a local maximum and minimum prior to the global PMF maximum, which occurs when a low number of lipids are initially extracted before a larger number are extracted in subsequent windows (discussed in more detail below); when this behavior was observed, an additional simulation replica was performed to ensure adequate sampling near the PMF maximum. As S further increases, all PMFs decrease due to a decrease in  $D_z$  and an increase in contacts that promote lipid extraction (state C in Figure 2). Large values of S correspond to NP adsorption to the upper leaflet of the bilayer with numerous extracted lipids stabilizing the adsorbed configuration (state D in Figure 2 with large  $D_z$  and a large number of contacts).

While all PMFs demonstrate qualitatively similar features, there are distinct quantitative differences depending upon the ligand R group. To explore these differences, we first define the adsorption free energy as the minimum value of the PMF as a function of S because this quantity reflects the free energy difference between state A (in solution) and state D (adsorbed to the upper leaflet of the bilayer); more negative values indicate that adsorption is more favorable. The adsorption free energies range between approximately -47  $k_BT$  to -202  $k_BT$ , indicating that adsorption is favorable for all NPs. The observation of lipid extraction for all NPs indicates that negative adsorption free energies are due to favorable hydrophobic interactions between ligands and extracted lipids, with differences in the adsorption free energies attributed to differences in electrostatic and hydrophobic interactions between ligand R groups and lipid head groups. Adsorption is least favorable for the C<sub>4</sub>SO<sub>3</sub> NP, which is expected given the weaker electrostatic interactions between lipid head groups and its zwitterionic R group compared to the cationic R groups for all other NPs. Adsorption is most favorable for the C<sub>1</sub>Bn NP which can be attributed to stronger cation- $\pi$  binding interactions.<sup>70</sup> For the remaining ligands with linear alkyl R groups, adsorption is more favorable for shorter, less lipophilic R groups (C<sub>1</sub>, C<sub>5</sub>, and C<sub>9</sub>) than longer, more lipophilic R groups (C<sub>13</sub> and C<sub>17</sub>). This result is counterintuitive, as more lipophilic R groups might be expected to promote adsorption; this behavior reflects the reduced free volume in the monolayers of NPs with long, lipophilic R groups due to interactions between ligand R groups and ligand backbones, as further elaborated upon below.<sup>71</sup> Despite these R group-specific differences in adsorption free energies, all adsorption free energies are sufficiently favorable that differences among predicted values would not influence experimentally observed adsorption behavior significantly. Therefore, we next focus on the values of the PMF maxima to understand if ligand R groups influence adsorption behavior by impacting free energy barriers to adsorption.

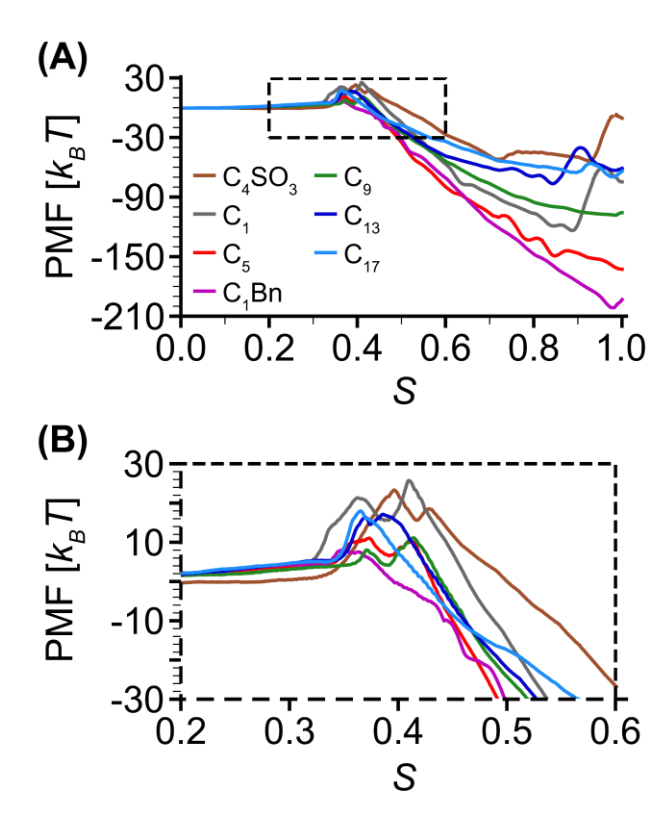


**Figure 3.** Potentials of mean force (PMFs) for the seven NPs with ligands shown in Figure 1B. PMFs are computed as a function of the distance along the MFEP, S. (A) Complete PMFs. (B) Enlarged PMFs to show differences in PMF maxima, which likewise indicate differences in free energy barriers of adsorption modulated by the physicochemical properties of the ligands and distinct NP-bilayer interaction mechanisms.

# Intercalation of ligand R group into the bilayer reduces free energy barrier for adsorption

Figure 3B presented enlarged portions of the PMFs corresponding to values of *S* where the PMFs reach maxima. This plot shows differences in PMF maxima for different ligand R groups that correspond to differences in the barriers to adsorption. Prior work has shown that free energy barriers for the insertion of lipophilic groups into bilayers, similar to the behavior observed in Figure 2, can be related to the formation of contacts with lipid tails. 63,71,72 Therefore, we further outline quantitative comparisons between the thermodynamics and the molecular mechanisms that modulate NP adsorption to the upper leaflet of the bilayer to elucidate the role of lipophilicity during this process. Specifically, Figure 4B shows the free energy barrier for adsorption (from the PMFs in Figure 3) for each NP and Figure 4C quantifies the number of contacts between different groups computed from the umbrella sampling window that is closest in CV space to the value of *S* corresponding to each PMF maximum. Comparing these values to each other and to simulation snapshots of the same umbrella sampling windows in Figure 4A identifies several relevant ligand-lipid interactions that characterize the adsorption process, as we next describe.

The C<sub>4</sub>SO<sub>3</sub> and C<sub>1</sub> NPs exhibit large free energy barriers of  $19.2 \pm 4.1 \ k_BT$  and  $24.0 \pm 3.6 \ k_BT$ , respectively. The ligands for these NPs have low lipophilicity and solvent-exposed charged groups, suggesting that the interactions with the bilayer are primarily driven by electrostatic interactions. Simulation snapshots (Figure 4A) reveal that the free energy barrier to adsorption for these NPs is associated with strong membrane deformation induced by the partitioning of lipid tail groups into the NP hydrophobic core from the hydrophobic bilayer bulk, which we refer to as "lipid protrusions." Lipid protrusions are promoted by hydrophobic interactions between the nonpolar groups in the ligand backbones and the tails of the lipids as shown by the large number of contacts between ligand backbone and lipid tail beads in Figure 4C. Because the R groups for these NPs are charged, lipid protrusions

require the lateral displacement of ligand R groups and lipid head groups, which interact with each other through Coulombic interactions as shown by the small number of contacts between ligand R groups and lipid tail groups in Figure 4C. The resulting "lipid bridge" structure that forms due to lipid protrusions (Figure 4A, and previously noted in Figure 2) resembles the high-energy stalk commonly observed during vesicle fusion. 51,73,74 This substantial bilayer disruption explains the large free energy barrier associated for adsorption of these NPs.

The  $C_5$  (11.7 ± 0.9  $k_BT$ ),  $C_1Bn$  (9.3 ± 1.6  $k_BT$ ), and  $C_9$  (11.2 ± 0.1  $k_BT$ ) NPs exhibit substantially lower free energy barriers compared to the  $C_4SO_3$  and  $C_1$  NPs. The ligands for these NPs are of intermediate lipophilicity, and the corresponding simulation snapshots in Figure 4A indicate that their R groups insert into the upper leaflet of the bilayer due to favorable hydrophobic interactions with lipid tails. These configurations are consistent with the low-energy ligand intercalation mechanism identified in prior AA simulations. Figure 4C indicates that intercalation primarily leads to contacts between the lipophilic R groups and lipid tail groups. While the  $C_9$  NP also has contacts between ligand backbones and lipid tails, no visible lipid protrusions are observed, and these contacts are instead generated by the intercalated R group pulling the NP core and lipid tails close together without extracting the lipids from the bilayer. The lack of notable bilayer disruption associated with ligand intercalation explains the lower adsorption barrier for these three NPs.

Surprisingly, the  $C_{13}$  (20.0 ± 4.0  $k_BT$ ) and  $C_{17}$  (15.6 ± 3.5  $k_BT$ ) NPs exhibit free energy barriers comparable to the  $C_4SO_3$  and  $C_1$  NPs that are larger than the free energy barriers for the  $C_5$  and  $C_9$  NPs, even though  $C_{13}$  and  $C_{17}$  NPs are coated with linear alkyl-terminated ligands that are longer and more lipophilic than the  $C_5$  and  $C_9$  NPs. This comparison indicates that there is a non-monotonic variation in the free energy barrier for adsorption as a function of ligand lipophilicity. Simulation snapshots indicate that unlike the  $C_5$ ,  $C_1Bn$ , and  $C_9$  NPs, the longer  $C_{13}$  and  $C_{17}$  R groups do not intercalate into the bilayer and instead lipid protrusions mediate contact with the NP as with the shorter  $C_1$  and  $C_5$  ligands, although the bilayer is noticeably less disrupted. Figure 4C confirms that both R groups and ligand backbones are in contact with tail groups, with the large number of backbone-tail group contacts consistent with lipid protrusions and the formation of a high-energy lipid bridge.

To explain the inability of the  $C_{13}$  and  $C_{17}$  R groups to intercalate in the bilayer, we hypothesized that hydrophobic interactions with ligand backbones cause the ligands to fold back and bury R groups within the ligand monolayer, where they are shielded from the surrounding solvent. This "backfolding" behavior inhibits the extension of the R out of the ligand monolayer and into contact with the lipid. To test this hypothesis, we explored the capacity of R groups from each NP to extend into solution by computing radial distribution functions (RDFs) from unbiased simulations of each NP in solution (i.e., in the absence of lipids). These unbiased simulations were equilibrated with isotropic pressure coupling as described in the SI, and then sampled every 10 ps during a 50 ns production trajectory. We expect that ligand backfolding would result in the charged quaternary ammonium being exposed to solvent, while the last bead of the R group would be close to the core of the NP. RDFs were thus computed for the quaternary ammonium and the last bead of the ligands using the center of mass of the NP as reference. Figure 5 compares these RDFs for six NPs excluding the C<sub>1</sub> NP (since its R group bead is the quaternary ammonium bead). The RDFs for the quaternary ammonium group and R group for the C<sub>4</sub>SO<sub>3</sub> NP overlap, indicating that the R group extends toward solution as expected due to its zwitterionic nature. RDFs for the more lipophilic ligands (C<sub>5</sub>, C<sub>1</sub>Bn, and C<sub>9</sub>) also overlap, albeit to a lesser degree, indicating that the R groups can extend appreciably into solution. In contrast, RDFs for the longer lipophilic ligands (C<sub>13</sub> and C<sub>17</sub>) show minimal overlap such that the R group is localized near the core of the NP. These results support the hypothesis that only the C<sub>13</sub> and C<sub>17</sub> R groups exhibit substantial backfolding, which explains their inability to intercalate into the bilayer.

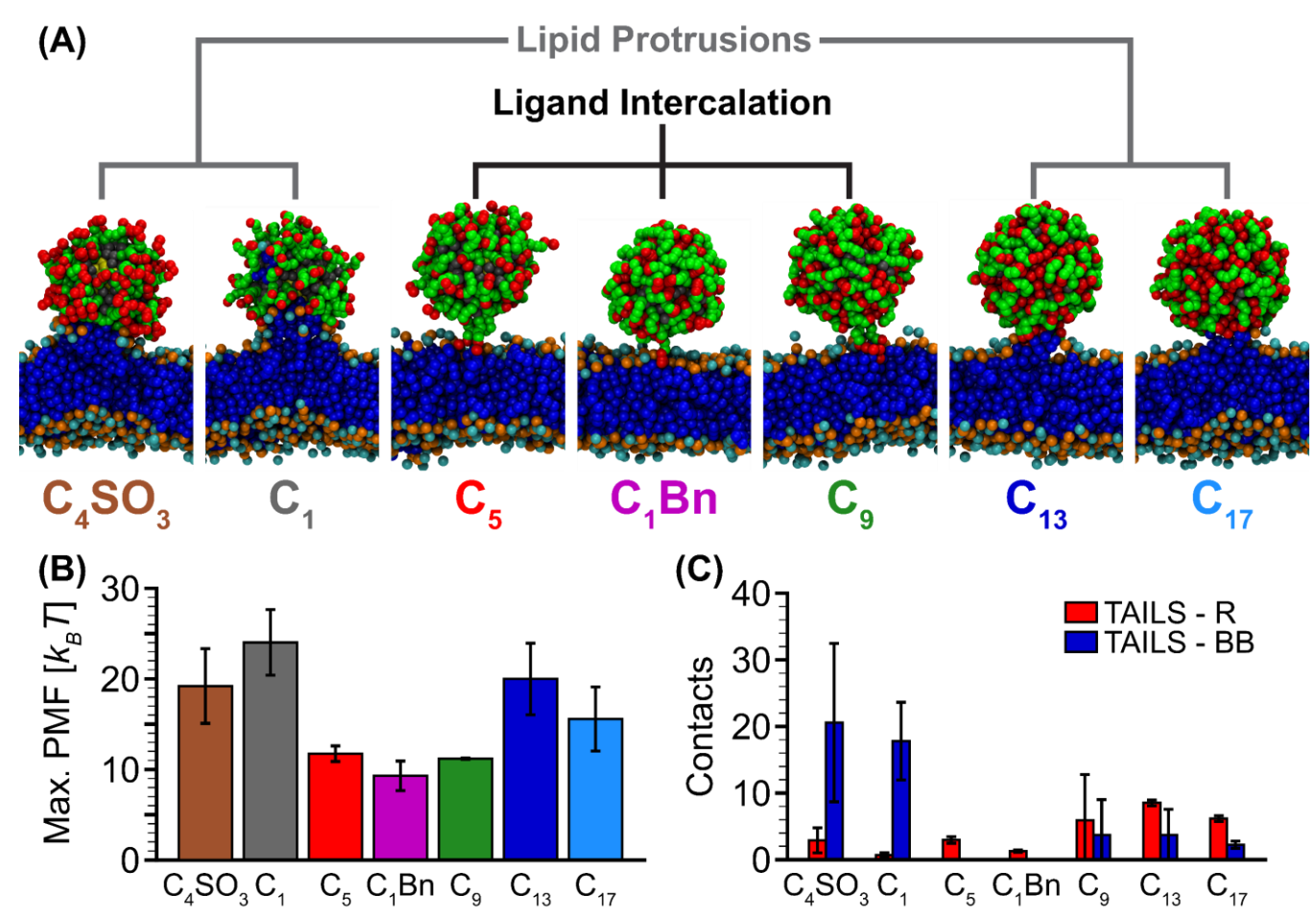


**Figure 4.** Comparison of free energy barriers to adsorption and ligand-lipid contacts. (A) Representative simulation snapshots of configurations from the umbrella sampling window corresponding to the free energy barrier for adsorption. The NP and lipids are color coded as described in Figure 1A. Water molecules and ions are not shown. Lipids from the bilayer that are in front of the center of mass of the NP and farther than 2.5 nm away from the S1 beads are not shown to visualize ligand intercalation in the bilayer and lipid extraction to the NP monolayer. (B) Maximum value of the PMF for each NP, which is defined as the free energy barrier of adsorption. (C) Contacts between lipid tails and either ligand R groups (TAILS - R) or ligand backbone groups (TAILS - BB). Contacts were computed from the same window used for the snapshots in (A). Error bars in (B) and (C) were calculated as the standard deviation between three replicas for C<sub>4</sub>SO<sub>3</sub> and C<sub>1</sub> NPs, and between two replicas for C<sub>5</sub>, C<sub>1</sub>Bn, C<sub>9</sub>, C<sub>13</sub>, and C<sub>17</sub> NPs.

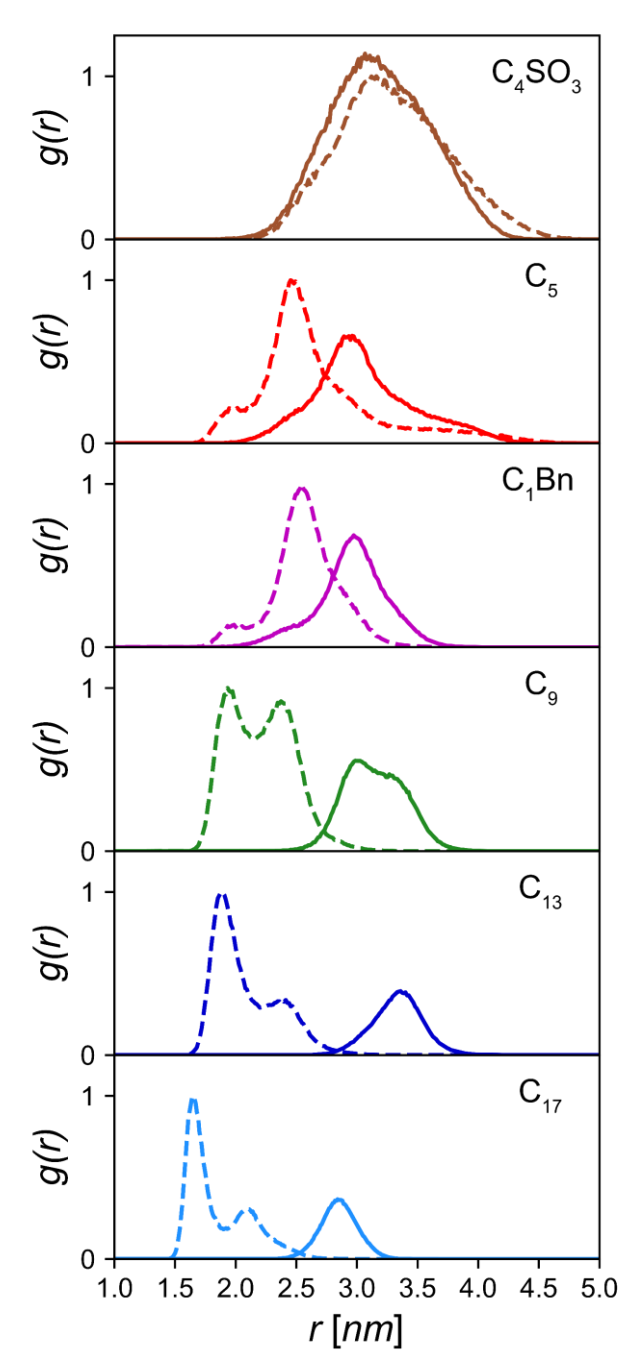


Figure 5. Radial distribution functions, g(r), computed for the quaternary ammonium bead (solid lines) and the last bead of each ligand R group (dashed lines) using the center of mass of the NP as reference. The RDF for the  $C_1Bn$  NP was computed with the center of mass of the benzene ring. All data were normalized using the maximum counts for the last bead and were computed from a single unbiased simulation of each NP in solvent. The gmx rdf tool was used with a bin size of 0.01 nm.

# Onset of lipid extraction coincides with free energy barrier for adsorption

To further quantify the relationship between lipid protrusions, lipid extraction, and free energy barriers for adsorption, Figure 6 compares values of  $D_z$ , contacts, and the number of lipids extracted computed for each umbrella window along the MFEP for one replica of the  $C_1$ ,  $C_1Bn$ , and  $C_{13}$  NPs, which are the NPs with the smallest ( $C_1Bn$ ) and two largest ( $C_1$  and  $C_{13}$ ) free energy barriers. We classify a lipid as being extracted when its phosphate group is coordinated to (i) at most one phosphate group of another lipid and (ii) at least one quaternary

ammonium of the NP ligands. The cut-off distance for phosphate-phosphate coordination was chosen as 1.1 nm from the radial distribution function of phosphate groups in a plain bilayer. The cut-off distance for the phosphate-ammonium coordination was chosen as 1.2 nm by matching the computed number of lipids extracted to the simulation snapshots; this cut-off consistently yielded good agreement between quantitative measurements and qualitative observations.

All three plots exhibit a similar increase in the PMF as  $D_z$  decreases prior to the formation of contacts with the bilayer. Upon the initial increase in contacts (near S=0.3), however, the  $C_1$  and  $C_{13}$  NPs show a sharp increase in the PMF. Both NPs exhibit similar features with the increase in the PMF and number of contacts coinciding with the initial extraction of lipids from the bilayer. The PMF maxima are reached at a larger value of S after more lipids are extracted. These behaviors are characteristic of initial lipid protrusions followed by substantial lipid extraction. One difference between the  $C_1$  and  $C_{13}$  NPs is the first local maximum observed for the  $C_1$  NP, which coincides with the first lipid being extracted (Figure 6A). Similar behavior is occasionally observed in other PMFs and is attributed to the stochastic nature of lipid extraction. In contrast to the behavior of the  $C_1$  and  $C_{13}$  NPs, the PMF maximum for the  $C_1$ Bn NP (Figure 6B) coincides with first lipid contacts and occurs with minimal lipid extraction. These behaviors are characteristic of ligand intercalation, which increases contacts without extracting lipids. Together, these observations quantify the extent of lipid extraction associated with lipid protrusions compared to ligand intercalation. Moreover, all NPs eventually extract lipids as the PMFs decrease, indicating that lipid extraction is a key factor in stabilizing NP adsorption. This prevalence of lipid extraction is consistent with prior studies that have shown the extraction of lipids to form a lipid corona around charged NPs. Terms of the protrusions compared to ligand intercalation of lipids to form a lipid corona around charged NPs.

Since lipid extraction refers specifically to lipids that are removed from the bilayer environment, the number of lipids extracted does not directly quantify the formation of a lipid bridge observed in the snapshot of the  $C_{13}$  NP in Figure 4A. The bilayer disruption associated with this lipid bridge is expected to contribute to the free energy barrier to adsorption. To more clearly highlight the bilayer disruption associated with the lipid bridge, Figure 6 shows the time-averaged number density of lipid beads from the umbrella sampling window corresponding to the maximum value of the PMF (*i.e.*, the same trajectory from which the snapshots in Figure 4A were obtained). These plots support the observation that the  $C_1$  and  $C_{13}$  NPs induce substantial bilayer deformations (visible from the high density of lipid beads at z-distances greater than 2 nm from the bilayer center) associated with high free energy barriers, whereas the bilayer is essentially unperturbed upon intercalation of the  $C_1$ Bn ligands. These NPs are also unable to move closer to the bilayer due to these lipid deformations, explaining the plateaus in  $D_z$  observed at higher values of S. The deformation for the  $C_{13}$  NP is less pronounced than for the  $C_1$  NP and consequently has a smaller free energy barrier. These densities explain the origin of the larger barrier for the  $C_{13}$  NP in comparison to the  $C_1$ Bn NP.

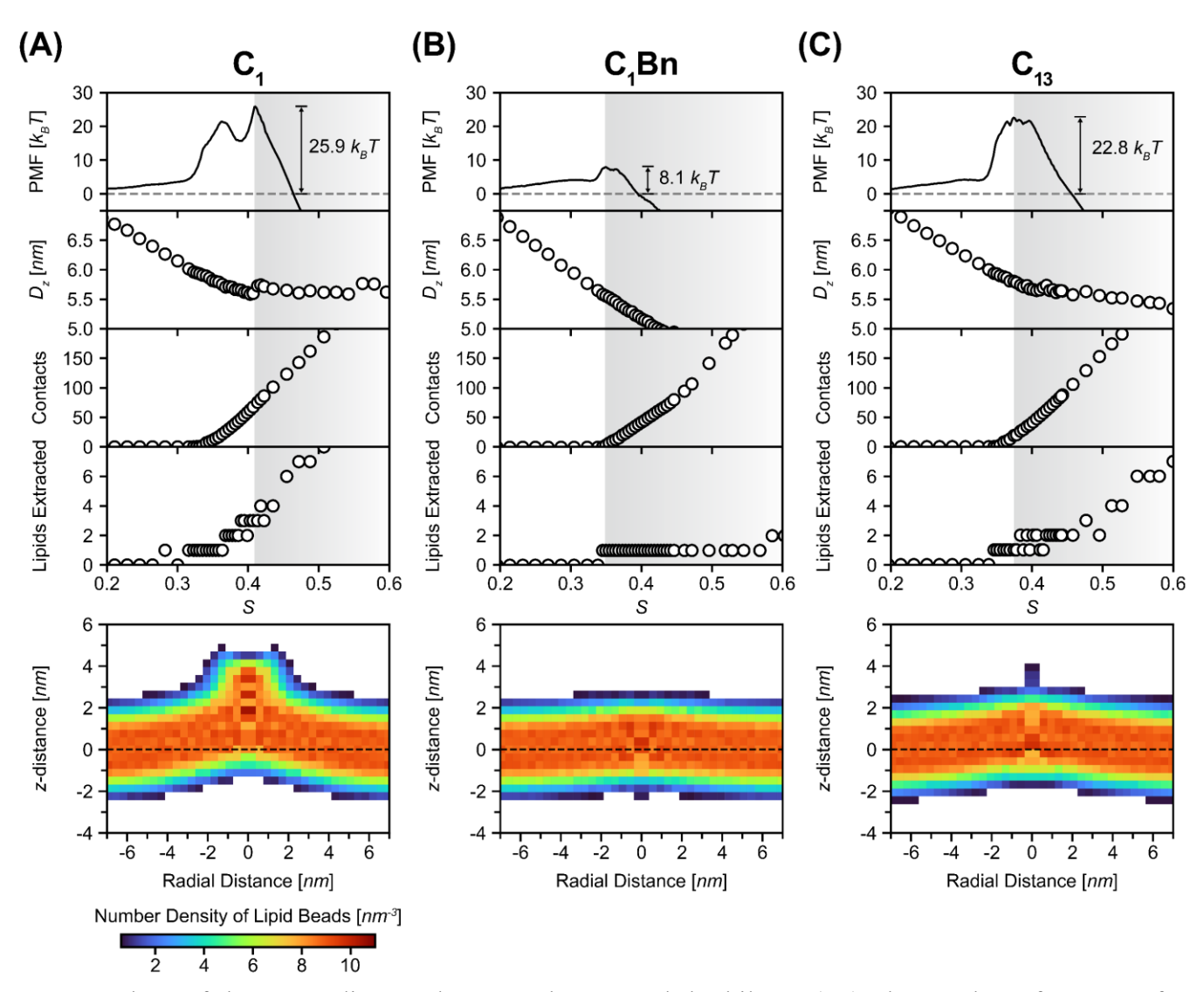


**Figure 6.** Values of the PMF, distance between the NP and the bilayer ( $D_z$ ), the number of contacts formed between the NP and the bilayer, and number of extracted lipids along the MFEP computed for the (A)  $C_1$ , (B)  $C_1Bn$ , and (C)  $C_{13}$  NPs. The shaded regions indicate values of S greater than the value that corresponds to the free energy barrier of adsorption. The plots at bottom show histograms of the time-averaged number density of all lipid beads as a function of the z-component of the distance from the bilayer center (z-distance) and the distance from the center of the NP in the x-y plane (radial distance). Histograms were generated from the same trajectories used to generate the snapshots in Figure 4A, which correspond to the maximum values of the PMFs for these NPs. Histogram bins were 0.375 nm in the radial direction and 0.375 nm in the z-direction. Densities for positive and negative radial distances are equivalent; negative distances are included for visualization purposes only. The bilayer center was computed as the center of mass of the phosphate group for lipids farther than 5 nm radially from the center of the NP.

# Ligand-specific adsorption mechanisms

Based on our observations, we propose three different mechanisms that modulate NP adsorption to the upper leaflet of the bilayer in Figure 7: lipid protrusions, ligand intercalation, and lipid protrusions with ligand backfolding. The lipid protrusions mechanism refers to the extension of lipid tail groups out of the bilayer and into the hydrophobic core of the NP to initiate irreversible adsorption. Lipid protrusions were observed for the C<sub>4</sub>SO<sub>3</sub> and C<sub>1</sub> NPs and led to large free energy barriers of adsorption because such protrusions are energetically unfavorable, <sup>51,79</sup> manifesting as minimal irreversible adsorption for similar NPs in experiments. <sup>63</sup> Ligand

intercalation refers to the extension of sufficiently long and lipophilic ligand R groups into the hydrophobic core of the lipid bilayer to promote hydrophobic contact with lipid tail groups. The intercalation mechanism led to the lowest free energy barriers of adsorption for the C<sub>5</sub>, C<sub>1</sub>Bn, and C<sub>9</sub> NPs, which were again observed experimentally to adsorb to the greatest extent.<sup>63</sup> Further increasing the length of the ligand R group to C<sub>13</sub> and C<sub>17</sub> unexpectedly led to lipid protrusion behavior with free energy barriers of adsorption comparable to C<sub>4</sub>SO<sub>3</sub> and C<sub>1</sub>. To explain this result, we identified ligand backfolding as a mechanism that competes against ligand intercalation because the preferential partitioning of sufficiently long ligand R groups within the ligand monolayer inhibits contact with the bilayer, requiring lipid protrusions to initiate hydrophobic contact. Ligand backfolding thus leads to the non-monotonic behavior in the adsorption free energy barrier with R group lipophilicity, as shown in Figure 4A.

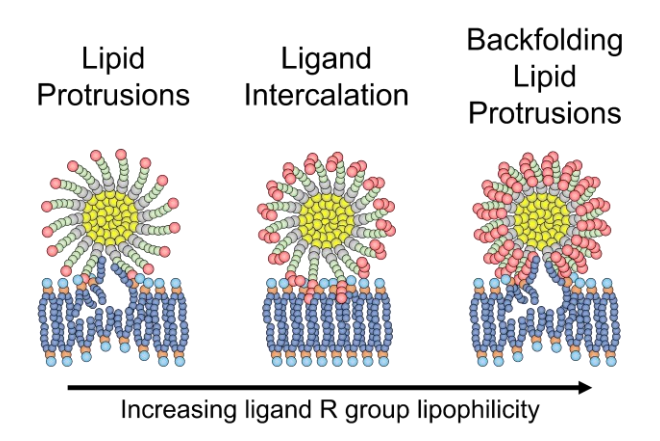


**Figure 7.** Schematic illustrations of the three mechanisms that determine the free energy of adsorption and how they depend upon ligand R group properties.

## **CONCLUSIONS**

In this work, we performed CG simulations to investigate the adsorption of seven different small (2 nm in diameter) ligand-functionalized, cationic gold NPs to single-component lipid bilayers. For similar NPs, prior experimental QCM-D measurements revealed that NP adsorption increased with increasing ligand R group lipophilicity and was reversible for NPs with short aliphatic R groups but (quasi)-irreversible for NPs with more lipophilic R groups (longer aliphatic groups or a benzyl group). 63 To understand mechanisms dictating these results, we performed CG simulations with metadynamics to determine the free energy landscape for NP adsorption as a function of two collective variables: the distance of the NP from the membrane and the number of NP-lipid contacts. The free energy landscape (Figure 2) reveals free energy changes associated with NP adsorption and desorption from the bilayer, with adsorption stabilized by the extraction of lipids from the bilayer and into the corona of the NP. Biasing two collective variables is necessary to resolve distinct adsorption (without extraction) and desorption (after extraction) regions of the free energy landscape. We further computed minimum free energy paths for adsorption and corresponding PMFs (Figure 3) to resolve adsorption free energies and free energy barriers for all seven NPs. All NPs exhibit highly favorable adsorption free energies consistent with irreversible adsorption. However, the adsorption free energy barrier depends upon ligand lipophilicity, indicating that experimentally observed differences in adsorption are a kinetic phenomenon. In particular, we find that the C<sub>5</sub>, C<sub>1</sub>Bn, and C<sub>9</sub> NPs have the lowest adsorption free energy barriers, which is consistent with experimental observations that similar NPs exhibit the most irreversible adsorption. 63 Surprisingly, however, increasing ligand lipophilicity further for the  $C_{13}$  and  $C_{17}$  increases the free energy for adsorption. We explain this nonmonotonic dependence of the adsorption free energy on ligand lipophilicity based on the three mechanisms proposed in Figure 7. Short, less lipophilic ligand R groups lead to NP adsorption through unfavorable lipid protrusions, ligand R groups of medium length and lipophilicity modulate adsorption through favorable ligand intercalation, and NPs

with long, highly lipophilic ligand R groups adsorb through unfavorable lipid protrusions due to backfolding mechanisms that prevent R group intercalation into the bilayer.

Together, these results suggest design considerations for nanomaterials and related soft materials that interact with lipid membranes. The finding of a nonmonotonic dependence of the free energy barrier of adsorption on R group lipophilicity due to backfolding highlights that simple descriptors of ligand R group properties are insufficient to capture the complex interplay of interactions at the nano-bio interface. A similar backfolding mechanism has also been shown by simulations to influence NP-protein interactions, <sup>35</sup> suggesting that this counterintuitive behavior generally influences nano-bio interactions. Simulation-derived descriptors, such as the NP-lipid contacts calculated here, may be better suited to capture the interactions between system components and used to guide NP design.<sup>25</sup> The results also suggest opportunities for separately tuning properties of the hydrophobic component of the ligand backbone (to modulate the free energy for irreversible adsorption) and the ligand R groups (to modulate the free energy barrier for adsorption). While here we investigated a limited set of R groups, future work will consider how a broader range of R group chemistries and structure, in combination with variations in core size, impact adsorption. We note that dozens of ligands with the modular chemical structure in Figure 1A have been synthesized previously, leading to a large feasible design space encompassing variations in R group length, bulkiness, lipophilicity, and charge.<sup>17,22,80,81</sup>

The molecular mechanisms and thermodynamics for adsorption explored in this work reflect interactions with single-component, zwitterionic lipid bilayers, which are commonly used as model cell membranes. <sup>46–48</sup> Biological membranes can contain numerous lipid components as well as distinct domains (*e.g.*, lipid rafts), which may influence NP-membrane interactions. <sup>30,55,56</sup> We expect the ligand-mediated adsorption mechanisms described in this work to generalize to adsorption on multicomponent membranes because they emerge from the ability of ligands to intercalate into the hydrophobic core of the bilayer or from ligand-ligand interactions, both factors that should be largely independent of membrane composition. Nonetheless, in future work we will study ligand-specific variations in NP adsorption to multicomponent lipid bilayers with components that influence the surface charge density (*e.g.*, anionic lipids) or fluidity (*e.g.*, cholesterol). Probing the mechanisms and thermodynamics of NP adsorption to such biomimetic multicomponent bilayers will provide valuable insight into developing these synthetic nanomaterials for applications in biotechnology and targeted drug delivery.

Finally, the definitions of the collective variables used in this work are appropriate for studying adsorption of a NP to one leaflet of the bilayer, but are not intended to bias the observation of rare events related to the translocation of charged ligand R groups across the bilayer.<sup>51–53,82</sup> Nonetheless, visual inspection of the umbrella sampling windows corresponding to *S* values near the second energetic barriers for some of the NPs revealed strong bilayer disruption. In the case of the strongly lipophilic NPs, at least one linear alkyl ligand translocated across the bilayer to the lower leaflet (Figure S34). Such processes may lead to the further insertion of the NP into the bilayer core and could be associated with biophysical processes such as non-disruptive cellular internalization.<sup>49</sup> Future work will thus extend the computational methodology developed here to also consider translocation processes to explore effects of ligand R groups on a wider variety of membrane interactions.

# **METHODS**

Coarse-grained molecular dynamics simulation parameters

All simulations were performed with GROMACS 2021.5<sup>83,84</sup> patched with PLUMED 2.8.0<sup>85</sup> using a leap-frog integrator with a timestep of 20 fs. The temperature was controlled at 300 K using the velocity-rescale thermostat. System equilibration was performed step-wise for a total of 45 ns in the *NPT* ensemble with semi-isotropic pressure coupling at 1 bar using a Berendsen barostat. Production runs were performed with the same parameters used for equilibration with the exception of using the Parrinello-Rahman barostat to control the pressure. A

detailed description of other simulation parameters is included in the SI and details for the production simulations are provided below.

Coarse-grained simulations were performed using the MARTINI force field<sup>86</sup> version 2.3P.<sup>70,87–89</sup> This version improves aromatics-choline interactions to reproduce membrane-binding events. We also used the refined polarizable water model to model electrostatic interactions more accurately.<sup>88,89</sup> The use of a polarizable water model improves the treatment of electrostatic interactions to satisfactorily capture behavior from more accurate all-atom (AA) simulations<sup>53,59</sup> and thus is suitable for analyzing adsorption behavior.

System description and coarse-grained model parameters

Following our previous work,<sup>63</sup> we modeled NP adsorption to a single-component zwitterionic lipid bilayer composed of DIPC, which is commonly used as a representation of DOPC in MARTINI simulations.<sup>90</sup> The initial bilayer was generated using the *insane.py* script<sup>91</sup> with dimensions of 14 nm ×14 nm × 24 nm and 289 lipids in each leaflet. After solvating the NP and the bilayer, the final number of water molecules ranged between 29,000 and 31,000 with 72 Cl<sup>-</sup> counterions to neutralize the cationic ligands; Table S1 reports exact numbers.

We modeled 2 nm diameter gold NPs coated with 72 ligands; this grafting density is based on the average number of ligands per NP measured experimentally for similar NPs. 17 The core of the NP was modeled as a spherical hollow shell following our prior work. 55,58 All ligands have the modular structure shown in Figure 1A. Each ligand consists of an undecane thiol segment, a tetraethylene glycol segment, and an R group. For the thiol segment, we modeled the S(CH<sub>2</sub>)<sub>3</sub> group as a C5 bead (using MARTINI naming conventions) and each (CH<sub>2</sub>)<sub>4</sub> group as a C1 bead. For the tetraethylene glycol segment, we modeled each ethylene oxide group using the EO bead model developed by Grunewald *et al.* 92 which has been shown to capture experimentally relevant NP-bilayer interactions in numerous past simulations. 50,52,53,55-57 We mapped the EO bead to each [O-CH<sub>2</sub>-CH<sub>2</sub>] group instead of its original [CH<sub>2</sub>-O-CH<sub>2</sub>] group. We chose this mapping to model the quaternary ammonium in the R group as a Q0 (choline) bead in which none of its carbon atoms are considered part of the R group beads. Keeping the original EO bead mapping would require a smaller 3:1 bead mapping for the undecane thiol segment.

Structures of the ligand R groups modeled in this study are shown in Figure 1B. R groups were selected based on our previous study and prior experimental studies to ensure that all R groups are experimentally relevant<sup>63,80</sup>. We modeled cationic ligands comprised of either linear alkanes or a benzyl group to study how R group lipophilicity modulates adsorption thermodynamics and mechanisms. We also modeled a zwitterionic ligand with 1-butanesulfanote bonded to the quaternary ammonium as an R group expected to exhibit a large free energy barrier for adsorption to zwitterionic bilayers. For the R groups, we modeled (CH<sub>2</sub>)<sub>4</sub> groups as C1 beads, the benzene ring as a cyclic moiety of three SC5 beads (quaternary ammonium bonded to a single SC5 bead that is bonded to the other two SC5 beads), and the 1-butanesulfonate group as an SC1 bead bonded to a Qda bead.<sup>35</sup> The lipophilicity of each R group was quantified by computing LogP values using Crippen's method<sup>93</sup> as implemented in ChemDraw 21.0.0 (reported in Figure 1B).

Bonded parameters for the ligands were obtained through a bottom-up parameterization approach using data obtained from molecular dynamics simulations using all-atom models of each NP coated with the same number of ligands and solvated in water. We chose to parameterize each ligand independently to capture potential effects on ligand conformations due to grafting to the gold core. Detailed descriptions of our parameterization are included in the SI (Figure S6-S11). The 72 ligands were distributed spherically and uniformly to generate the NP, and all C5 beads were bonded to their nearest C5 neighbors within 1.24 nm with a harmonic potential of 5,000 kJ/mol·nm² to ensure the stability and rigidity of the core.

Definition of collective variables for free energy calculations

We defined two CVs,  $D_z$  and contacts, to describe NP adsorption to the bilayer as schematically shown in Figure 1C.  $D_z$  quantifies the distance in the z dimension between the center of mass of the NP (including its ligands) and the center of mass of 20 randomly selected lipids from the bilayer (10 from the upper leaflet and 10 from the lower leaflet).  $D_z$  is reported either as a distance in units of nm or as a unitless value that is scaled by the z-dimension of the simulation box. For metadynamics calculations, we sampled  $D_z$  in nm, while for free energy calculations we used  $D_z$  as a unitless value to ensure appropriate biasing of the CVs regardless of possible bilayer or box size changes during sampling. Contacts quantify the number of CG beads from one set of beads that are within 0.47 nm (the standard diameter of MARTINI beads) of any bead from another set of beads. For metadynamics and free energy calculations, a contact was counted when any NP bead was within the specified cutoff of any lipid bead. For other analyses, a contact was defined between specific subgroups of beads: ligand backbone beads and lipid tail beads, ligand R group beads and lipid tail beads. All CVs were computed using the DISTANCE ( $D_z$ ) and COORDINATION (contacts) collective variables in PLUMED 2.8.085.

### 2D Metadynamics

We performed 2D well-tempered metadynamics<sup>69</sup> to approximate the free energy landscape for NP adsorption to the bilayer as a function of  $D_z$  and contacts. These simulations were initiated with the NP far from the bilayer. The two CVs were biased using two-dimensional Gaussian hills with a height of 0.2 kJ/mol and width of 0.2 nm for  $D_z$  and 1 contact. Hills were deposited every 20 steps (400 ps) during a 500 ns simulation with a bias factor of 10 kJ/mol. Four walkers were sampled simultaneously for a total of 2  $\mu$ s of sampling time. To avoid sampling configurations with large  $D_z$  (i.e., with the NP diffusing in solution far from the bilayer), we imposed an upper wall on the scaled value of  $D_z$  at 0.40 with a harmonic potential of 150,000 kJ/mol. The contacts sampled were those between all NP beads and all lipid beads. Metadynamics was only performed for the  $C_1$  NP with convergence shown in Figure S12.

# String method with swarms of trajectories

We used the string method with swarms of trajectories  $^{64-66}$  to compute the minimum free energy path (MFEP) for NP adsorption to the bilayer as a function of  $D_z$  and contacts. We chose the initial string for each MFEP as the pathway that connects two states, the NP in solution and the NP adsorbed to the upper leaflet of the bilayer, which are expected to represent stable equilibrium states (Figure 2). Each string was comprised of 24 evenly spaced independent windows. Restrained simulations were performed to equilibrate the CVs and generate a set of 128 independent configurations (from each restrained simulation) that were subsequently used to generate 24 swarms of unbiased simulations (*i.e.*, the swarms of trajectories). The average drift computed from the unbiased trajectories for each window was added to the old CVs to evolve the string. A new string was generated by linearly interpolating through the new sets of CVs and reparameterized to ensure equal distances between consecutive windows. A total of 75 iterations were required to achieve convergence (Figure S14-S20). Since the string method with swarms of trajectories is a finite-temperature method, the final path fluctuates slightly every iteration even after convergence. Therefore, we determined the MFEP by averaging the last five strings using a spline fit. A more detailed description along with a schematic depicting this method are shown in the SI.

#### Umbrella sampling simulations

We performed 1D umbrella sampling to compute the PMF as a function of the distance along the MFEP. We used the path CV equations defined by Branduardi *et al.*<sup>67</sup> to define the distance along the path, S, and the normal distance away from the path, Z. The MFEP was discretized into 72 windows evenly spaced in S. Each umbrella sampling window was restrained at a chosen value of S using strong harmonic potentials near the region between where the NP begins making contacts with the bilayer and where the adsorption process begins; weak harmonic potentials were used for all other values of S. The values of these restraints were slightly varied for each NP and

for each replica to ensure numerical stability, particularly for cases in which the NP interacted very strongly with the bilayer (*i.e.*, due to strong lipid extraction and NP desorption). The restrained values of S and their corresponding spring constants are included in the SI. In all simulations, the value of Z was restrained at 0.02 using a harmonic potential of 20,000,000 kJ/mol to restrict sampling to the MFEP. For each window, we performed a 50 ns production run and discarded the first 5 ns as equilibration. The last 45 ns were used to compute the PMF in terms of S using the Weighted Histogram Analysis Method (WHAM)<sup>94</sup>. For the C<sub>4</sub>SO<sub>3</sub> NP, we discarded the first 10 ns as equilibration and used the last 40 ns for analyses. WHAM was performed as a function of both S and Z, with the final PMF reweighted to be a function of S only. To ensure robustness, the string method and umbrella sampling were repeated at least once for all NPs to ensure fully independent strings and PMFs between replicas. Due to the computational expense, two replicas were performed for all NPs and an additional replica (with a new string) was performed for NPs that exhibited instability during umbrella sampling (described in the SI).

#### **ACKNOWLEDGEMENTS**

This material is based upon work supported by the National Science Foundation under awards DMR-2044997 and MCB-1817292. R.C.V.L. also acknowledges support from the Vilas Trust through the Vilas Associates Award, provided by the Office of the Vice Chancellor for Research and Graduate Education at the University of Wisconsin-Madison. This work used the Advanced Cyberinfrastructure Coordination Ecosystem: Services & Support (ACCESS), which is supported by the National Science Foundation under Grant No. 2138307. C.A.H.Z and R.C.V.L. acknowledge the support provided by the Graduate Engineering Research Scholars – Advanced Opportunity Fellowship from the University of Wisconsin – Madison, the Chemistry-Biology Interface Training Program (5T32GM008505-29), funded by the National Institute of General Medicine Sciences, from the University of Wisconsin – Madison, and the National Science Foundation through a Graduate Research Fellowship.

#### **SUPPORTING INFORMATION**

34 figures, 1 table, and additional information on the computational workflow, data supporting the convergence of simulation quantities, additional data for replicas of the computational workflow, GROMACS structure and topology files for the coarse-grained models of the NPs studied, and a spreadsheet with information on all simulation conditions to facilitate reproducibility.

## **REFERENCES**

- (1) Huang, X.; Jain, P. K.; El-Sayed, I. H.; El-Sayed, M. A. Gold Nanoparticles: Interesting Optical Properties and Recent Applications in Cancer Diagnostics and Therapy. *Nanomedicine-UK* **2007**, *2* (5), 681–693.
- (2) Gao, X.; Cui, Y.; Levenson, R. M.; Chung, L. W. K.; Nie, S. In Vivo Cancer Targeting and Imaging with Semiconductor Quantum Dots. *Nat Biotechnol* **2004**, *22* (8), 969–976.
- (3) Ghosh, P.; Han, G.; De, M.; Kim, C. K.; Rotello, V. M. Gold Nanoparticles in Delivery Applications. *Adv Drug Deliv Rev* **2008**, *60* (11), 1307–1315.
- (4) Sun, T.; Zhang, Y. S.; Pang, B.; Hyun, D. C.; Yang, M.; Xia, Y. Engineered Nanoparticles for Drug Delivery in Cancer Therapy. *Angewandte Chemie International Edition* **2014**, *53* (46), 12320–12364.
- (5) O'Neal, D. P.; Hirsch, L. R.; Halas, N. J.; Payne, J. D.; West, J. L. Photo-Thermal Tumor Ablation in Mice Using near Infrared-Absorbing Nanoparticles. *Cancer Lett* **2004**, *209* (2), 171–176.
- (6) Mout, R.; Moyano, D. F.; Rana, S.; Rotello, V. M. Surface Functionalization of Nanoparticles for Nanomedicine. *Chem Soc Rev* **2012**, *41* (7), 2539–2544.
- (7) Giljohann, D. A.; Seferos, D. S.; Daniel, W. L.; Massich, M. D.; Patel, P. C.; Mirkin, C. A. Gold Nanoparticles for Biology and Medicine. *Angewandte Chemie International Edition* **2010**, *49* (19), 3280–3294.
- (8) Alkilany, A. M.; Lohse, S. E.; Murphy, C. J. The Gold Standard: Gold Nanoparticle Libraries to Understand the Nano-Bio Interface. *Acc Chem Res* **2013**, *46* (3), 650–661.
- (9) Verma, A.; Stellacci, F. Effect of Surface Properties on Nanoparticle–Cell Interactions. *Small* **2010**, *6* (1), 12–21.
- (10) Goddard, Z. R.; Marín, M. J.; Russell, D. A.; Searcey, M. Active Targeting of Gold Nanoparticles as Cancer Therapeutics. *Chem Soc Rev* **2020**, *49* (23), 8774–8789.
- (11) Huang, R.; Luther, D. C.; Zhang, X.; Gupta, A.; Tufts, S. A.; Rotello, V. M. Engineering the Interface between Inorganic Nanoparticles and Biological Systems through Ligand Design. *Nanomaterials* **2021**, *11* (4), 1001.
- (12) Heinz, H.; Pramanik, C.; Heinz, O.; Ding, Y.; Mishra, R. K.; Marchon, D.; Flatt, R. J.; Estrela-Lopis, I.; Llop, J.; Moya, S.; Ziolo, R. F. Nanoparticle Decoration with Surfactants: Molecular Interactions, Assembly, and Applications. *Surf Sci Rep* **2017**, *72* (1), 1–58.
- (13) Love, J. C.; Estroff, L. A.; Kriebel, J. K.; Nuzzo, R. G.; Whitesides, G. M. Self-Assembled Monolayers of Thiolates on Metals as a Form of Nanotechnology. *Chem Rev* **2005**, *105* (4), 1103–1169.
- (14) Hong, R.; Fischer, N. O.; Verma, A.; Goodman, C. M.; Emrick, T.; Rotello, V. M. Control of Protein Structure and Function through Surface Recognition by Tailored Nanoparticle Scaffolds. *J Am Chem Soc* **2004**, *126* (3), 739–743.
- (15) Pengo, P.; Şologan, M.; Pasquato, L.; Guida, F.; Pacor, S.; Tossi, A.; Stellacci, F.; Marson, D.; Boccardo, S.; Pricl, S.; Posocco, P. Gold Nanoparticles with Patterned Surface Monolayers for Nanomedicine: Current Perspectives. *European Biophysics Journal* **2017**, *46* (8), 749–771.

- (16) Bai, X.; Wang, S.; Yan, X.; Zhou, H.; Zhan, J.; Liu, S.; Sharma, V. K.; Jiang, G.; Zhu, H.; Yan, B. Regulation of Cell Uptake and Cytotoxicity by Nanoparticle Core under the Controlled Shape, Size, and Surface Chemistries. *ACS Nano* **2020**, *14* (1), 289–302.
- (17) Jiang, Y.; Huo, S.; Mizuhara, T.; Das, R.; Lee, Y. W.; Hou, S.; Moyano, D. F.; Duncan, B.; Liang, X. J.; Rotello, V. M. The Interplay of Size and Surface Functionality on the Cellular Uptake of Sub-10 Nm Gold Nanoparticles. *ACS Nano* **2015**, *9* (10), 9986–9993.
- (18) Goodman, C. M.; McCusker, C. D.; Yilmaz, T.; Rotello, V. M. Toxicity of Gold Nanoparticles Functionalized with Cationic and Anionic Side Chains. *Bioconjug Chem* **2004**, *15* (4), 897–900.
- (19) Carnovale, C.; Bryant, G.; Shukla, R.; Bansal, V. Identifying Trends in Gold Nanoparticle Toxicity and Uptake: Size, Shape, Capping Ligand, and Biological Corona. *ACS Omega* **2019**, *4* (1), 242–256.
- (20) Li, X.; Robinson, S. M.; Gupta, A.; Saha, K.; Jiang, Z.; Moyano, D. F.; Sahar, A.; Riley, M. A.; Rotello, V. M. Functional Gold Nanoparticles as Potent Antimicrobial Agents against Multi-Drug-Resistant Bacteria. *ACS Nano* **2014**, *8* (10), 10682–10686.
- (21) Zheng, K.; Setyawati, M. I.; Leong, D. T.; Xie, J. Surface Ligand Chemistry of Gold Nanoclusters Determines Their Antimicrobial Ability. *Chemistry of Materials* **2018**, *30* (8), 2800–2808.
- (22) Moyano, D. F.; Liu, Y.; Peer, D.; Rotello, V. M. Modulation of Immune Response Using Engineered Nanoparticle Surfaces. *Small* **2016**, *12* (1), 76–82.
- (23) Dykman, L. A.; Khlebtsov, N. G. Immunological Properties of Gold Nanoparticles. *Chem Sci* **2017**, *8* (3), 1719–1735.
- (24) Wang, W.; Sedykh, A.; Sun, H.; Zhao, L.; Russo, D. P.; Zhou, H.; Yan, B.; Zhu, H. Predicting Nano-Bio Interactions by Integrating Nanoparticle Libraries and Quantitative Nanostructure Activity Relationship Modeling. *ACS Nano* **2017**, *11* (12), 12641–12649.
- (25) Chew, A. K.; Pedersen, J. A.; Van Lehn, R. C. Predicting the Physicochemical Properties and Biological Activities of Monolayer-Protected Gold Nanoparticles Using Simulation-Derived Descriptors. *ACS Nano* **2022**, *16* (4), 6282–6292.
- (26) Bigdeli, A.; Hormozi-Nezhad, M. R.; Parastar, H. Using Nano-QSAR to Determine the Most Responsible Factor(s) in Gold Nanoparticle Exocytosis. *RSC Adv* **2015**, *5* (70), 57030–57037.
- (27) Yan, X.; Sedykh, A.; Wang, W.; Yan, B.; Zhu, H. Construction of a Web-Based Nanomaterial Database by Big Data Curation and Modeling Friendly Nanostructure Annotations. *Nat Commun* **2020**, *11* (1), 1–10.
- (28) Oh, Y.; Cui, Q. Non-Equilibrium Transport of Nanoparticles across the Lipid Membrane. *Nanoscale* **2023**, *15* (29), 12307–12318.
- (29) Kariuki, R.; Penman, R.; Bryant, S. J.; Orrell-Trigg, R.; Meftahi, N.; Crawford, R. J.; McConville, C. F.; Bryant, G.; Voïtchovsky, K.; Conn, C. E.; Christofferson, A. J.; Elbourne, A. Behavior of Citrate-Capped Ultrasmall Gold Nanoparticles on a Supported Lipid Bilayer Interface at Atomic Resolution. *ACS Nano* **2022**, *16* (10), 17179–17196.
- (30) Pfeiffer, T.; De Nicola, A.; Montis, C.; Carlà, F.; Van Der Vegt, N. F. A.; Berti, D.; Milano, G. Nanoparticles at Biomimetic Interfaces: Combined Experimental and Simulation Study on Charged Gold Nanoparticles/Lipid Bilayer Interfaces. *Journal of Physical Chemistry Letters* **2019**, *10* (2), 129–137.

- (31) Foreman-Ortiz, I. U.; Liang, D.; Laudadio, E. D.; Calderin, J. D.; Wu, M.; Keshri, P.; Zhang, X.; Schwartz, M. P.; Hamers, R. J.; Rotello, V. M.; Murphy, C. J.; Cui, Q.; Pedersen, J. A. Anionic Nanoparticle-Induced Perturbation to Phospholipid Membranes Affects Ion Channel Function. *Proc Natl Acad Sci U S A* **2020**, *117* (45), 27854–27861.
- (32) Chew, A. K.; Dallin, B. C.; Van Lehn, R. C. The Interplay of Ligand Properties and Core Size Dictates the Hydrophobicity of Monolayer-Protected Gold Nanoparticles. *ACS Nano* **2021**, *15* (3), 4534–4545.
- (33) Chew, A. K.; Van Lehn, R. C. Effect of Core Morphology on the Structural Asymmetry of Alkanethiol Monolayer-Protected Gold Nanoparticles. *Journal of Physical Chemistry C* **2018**, *122* (45), 26288–26297.
- (34) Hoff, S. E.; Di Silvio, D.; Ziolo, R. F.; Moya, S. E.; Heinz, H. Patterning of Self-Assembled Monolayers of Amphiphilic Multisegment Ligands on Nanoparticles and Design Parameters for Protein Interactions. *ACS Nano* **2022**, *16* (6), 8766–8783.
- (35) Simonelli, F.; Rossi, G.; Monticelli, L. Role of Ligand Conformation on Nanoparticle-Protein Interactions. *Journal of Physical Chemistry B* **2019**, *123* (8), 1764–1769.
- (36) Liang, D.; Dahal, U.; Wu, M.; Murphy, C. J.; Cui, Q. Ligand Length and Surface Curvature Modulate Nanoparticle Surface Heterogeneity and Electrostatics. *Journal of Physical Chemistry C* **2020**, *124* (44), 24513–24525.
- (37) Chong, G.; Foreman-Ortiz, I. U.; Wu, M.; Bautista, A.; Murphy, C. J.; Pedersen, J. A.; Hernandez, R. Defects in Self-Assembled Monolayers on Nanoparticles Prompt Phospholipid Extraction and Bilayer-Curvature-Dependent Deformations. *Journal of Physical Chemistry C* **2019**, *123* (45), 27951–27958.
- (38) Yang, Y.; Qin, H.; Jiang, M.; Lin, L.; Fu, T.; Dai, X.; Zhang, Z.; Niu, Y.; Cao, H.; Jin, Y.; Zhao, F.; Peng, X. Entropic Ligands for Nanocrystals: From Unexpected Solution Properties to Outstanding Processability. *Nano Lett* **2016**, *16* (4), 2133–2138.
- (39) Gabellini, C.; Şologan, M.; Pellizzoni, E.; Marson, D.; Daka, M.; Franchi, P.; Bignardi, L.; Franchi, S.; Posel, Z.; Baraldi, A.; Pengo, P.; Lucarini, M.; Pasquato, L.; Posocco, P. Spotting Local Environments in Self-Assembled Monolayer-Protected Gold Nanoparticles. *ACS Nano* **2022**, *16* (12), 20902–20914.
- (40) Prud, M. V.; Kyrychenko, A.; Kalugin, O. N. PH-Controllable Coating of Silver Nanoparticles with PMMA- b -PDMAEMA Oligomers: A Molecular Dynamics Simulation Study. *The Journal of Physical Chemistry C* **2023**, *127* (24), 11748–11759.
- (41) Nel, A. E.; Mädler, L.; Velegol, D.; Xia, T.; Hoek, E. M. V.; Somasundaran, P.; Klaessig, F.; Castranova, V.; Thompson, M. Understanding Biophysicochemical Interactions at the Nano–Bio Interface. *Nat Mater* **2009**, *8* (7), 543–557.
- (42) Albanese, A.; Tang, P. S.; Chan, W. C. W. The Effect of Nanoparticle Size, Shape, and Surface Chemistry on Biological Systems. *Annu Rev Biomed Eng* **2012**, *14*, 1–16.
- (43) Chen Xie; Lin Zhang. Design and Characterization of Antithrombotic ClEKnsTy-Au Nanoparticles as Diagnostic and Therapeutic Reagents. *Physical Chemistry Chemical Physics* **2023**.
- (44) Lesniak, A.; Salvati, A.; Santos-Martinez, M. J.; Radomski, M. W.; Dawson, K. A.; Åberg, C. Nanoparticle Adhesion to the Cell Membrane and Its Effect on Nanoparticle Uptake Efficiency. *J Am Chem Soc* **2013**, *135* (4), 1438–1444.

- (45) Kim, S. T.; Saha, K.; Kim, C.; Rotello, V. M. The Role of Surface Functionality in Determining Nanoparticle Cytotoxicity. *Acc Chem Res* **2013**, *46* (3), 681–691.
- (46) Farnoud, A. M.; Nazemidashtarjandi, S. Emerging Investigator Series: Interactions of Engineered Nanomaterials with the Cell Plasma Membrane; What Have We Learned from Membrane Models? *Environ Sci Nano* **2019**, *6* (1), 13–40.
- (47) Rascol, E.; Devoisselle, J. M.; Chopineau, J. The Relevance of Membrane Models to Understand Nanoparticles—Cell Membrane Interactions. *Nanoscale* **2016**, *8* (9), 4780–4798.
- (48) Chen, K. L.; Bothun, G. D. Nanoparticles Meet Cell Membranes: Probing Nonspecific Interactions Using Model Membranes. *Environ Sci Technol* **2014**, *48* (2), 873–880.
- (49) Van Lehn, R. C.; Atukorale, P. U.; Carney, R. P.; Yang, Y. S.; Stellacci, F.; Irvine, D. J.; Alexander-Katz, A. Effect of Particle Diameter and Surface Composition on the Spontaneous Fusion of Monolayer-Protected Gold Nanoparticles with Lipid Bilayers. *Nano Lett* **2013**, *13* (9), 4060–4067.
- (50) Lolicato, F.; Joly, L.; Martinez-Seara, H.; Fragneto, G.; Scoppola, E.; Baldelli Bombelli, F.; Vattulainen, I.; Akola, J.; Maccarini, M. The Role of Temperature and Lipid Charge on Intake/Uptake of Cationic Gold Nanoparticles into Lipid Bilayers. *Small* **2019**, *15* (23), 1805046.
- (51) Van Lehn, R. C.; Alexander-Katz, A. Pathway for Insertion of Amphiphilic Nanoparticles into Defect-Free Lipid Bilayers from Atomistic Molecular Dynamics Simulations. *Soft Matter* **2015**, *11* (16), 3165–3175.
- (52) Simonelli, F.; Bochicchio, D.; Ferrando, R.; Rossi, G. Monolayer-Protected Anionic Au Nanoparticles Walk into Lipid Membranes Step by Step. *Journal of Physical Chemistry Letters* **2015**, *6* (16), 3175–3179.
- (53) Salassi, S.; Simonelli, F.; Bochicchio, D.; Ferrando, R.; Rossi, G. Au Nanoparticles in Lipid Bilayers: A Comparison between Atomistic and Coarse-Grained Models. *Journal of Physical Chemistry C* **2017**, *121* (20), 10927–10935.
- (54) Sun, L.; Cao, Y.; Chen, X.; Liang, Q. Interactions between Amphiphilic Nanoparticles Coated with Striped Hydrophilic/Hydrophobic Ligands and a Lipid Bilayer. *Commun Theor Phys* **2023**, *75* (6), 065601.
- (55) Sheavly, J. K.; Pedersen, J. A.; Van Lehn, R. C. Curvature-Driven Adsorption of Cationic Nanoparticles to Phase Boundaries in Multicomponent Lipid Bilayers. *Nanoscale* **2019**, *11* (6), 2767–2778.
- (56) Lin, X.; Lin, X. Surface Ligand Rigidity Modulates Lipid Raft Affinity of Ultra-Small Hydrophobic Nanoparticles: Insights from Molecular Dynamics Simulations. *Nanoscale* **2021**, *13* (21), 9825–9833.
- (57) Chen, X.; Tieleman, D. P.; Liang, Q. Modulating Interactions between Ligand-Coated Nanoparticles and Phase-Separated Lipid Bilayers by Varying the Ligand Density and the Surface Charge. *Nanoscale* **2018**, *10* (5), 2481–2491.
- (58) Sheavly, J. K.; Van Lehn, R. C. Bilayer-Mediated Assembly of Cationic Nanoparticles Adsorbed to Lipid Bilayers: Insights from Molecular Simulations. *AIChE Journal* **2020**, *66* (12), e16993.
- (59) Das, M.; Dahal, U.; Mesele, O.; Liang, D.; Cui, Q. Molecular Dynamics Simulation of Interaction between Functionalized Nanoparticles with Lipid Membranes: Analysis of Coarse-Grained Models. *Journal of Physical Chemistry B* **2019**, *123* (49), 10547–10561.

- (60) Shen, Z.; Baker, W.; Ye, H.; Li, Y. PH-Dependent Aggregation and PH-Independent Cell Membrane Adhesion of Monolayer-Protected Mixed Charged Gold Nanoparticles. *Nanoscale* **2019**, *11* (15), 7371–7385.
- (61) Lunnoo, T.; Assawakhajornsak, J.; Ruangchai, S.; Puangmali, T. Role of Surface Functionalization on Cellular Uptake of AuNPs Characterized by Computational Microscopy. *Journal of Physical Chemistry B* **2020**, *124* (10), 1898–1908.
- (62) Quan, X.; Zhao, D.; Li, L.; Zhou, J. Understanding the Cellular Uptake of PH-Responsive Zwitterionic Gold Nanoparticles: A Computer Simulation Study. *Langmuir* **2017**, *33* (50), 14480–14489.
- (63) Lochbaum, C. A.; Chew, A. K.; Zhang, X.; Rotello, V.; Van Lehn, R. C.; Pedersen, J. A. Lipophilicity of Cationic Ligands Promotes Irreversible Adsorption of Nanoparticles to Lipid Bilayers. *ACS Nano* **2021**, *15* (4), 6562–6572.
- (64) Pan, A. C.; Sezer, D.; Roux, B. Finding Transition Pathways Using the String Method with Swarms of Trajectories. *Journal of Physical Chemistry B* **2008**, *112* (11), 3432–3440.
- (65) Patel, S. J.; Van Lehn, R. C. Analysis of Charged Peptide Loop-Flipping across a Lipid Bilayer Using the String Method with Swarms of Trajectories. *Journal of Physical Chemistry B* **2021**, *125* (22), 5862–5873.
- (66) Maragliano, L.; Roux, B.; Vanden-Eijnden, E. Comparison between Mean Forces and Swarms-of-Trajectories String Methods. *J Chem Theory Comput* **2014**, *10* (2), 524–533.
- (67) Branduardi, D.; Gervasio, F. L.; Parrinello, M. From A to B in Free Energy Space. *Journal of Chemical Physics* **2007**, *126* (5), 54103.
- (68) Humphrey, W.; Dalke, A.; Schulten, K. VMD: Visual Molecular Dynamics. *J Mol Graph* **1996**, *14* (1), 33–38.
- (69) Laio, A.; Parrinello, M. Escaping Free-Energy Minima. *Proc Natl Acad Sci U S A* **2002**, *99* (20), 12562–12566.
- (70) Khan, H. M.; Souza, P. C. T.; Thallmair, S.; Barnoud, J.; De Vries, A. H.; Marrink, S. J.; Reuter, N. Capturing Choline-Aromatics Cation-π Interactions in the MARTINI Force Field. *J Chem Theory Comput* 2020, 16 (4), 2550–2560.
- (71) Rogers, J. R.; Geissler, P. L. Breakage of Hydrophobic Contacts Limits the Rate of Passive Lipid Exchange between Membranes. *Journal of Physical Chemistry B* **2020**, *124* (28), 5884–5898.
- (72) Van Lehn, R. C.; Alexander-Katz, A. Membrane-Embedded Nanoparticles Induce Lipid Rearrangements Similar to Those Exhibited by Biological Membrane Proteins. *Journal of Physical Chemistry B* **2014**, *118* (44), 12586–12598.
- (73) Kasson, P. M.; Lindahl, E.; Pande, V. S. Atomic-Resolution Simulations Predict a Transition State for Vesicle Fusion Defined by Contact of a Few Lipid Tails. *PLoS Comput Biol* **2010**, *6* (6), 1000829.
- (74) Brosio, G.; Rossi, G.; Bochicchio, D. Nanoparticle-Induced Biomembrane Fusion: Unraveling the Effect of Core Size on Stalk Formation. *Nanoscale Adv* **2023**, *5* (18), 4675–4680.
- (75) Olenick, L. L.; Troiano, J. M.; Vartanian, A.; Melby, E. S.; Mensch, A. C.; Zhang, L.; Hong, J.; Mesele, O.; Qiu, T.; Bozich, J.; Lohse, S.; Zhang, X.; Kuech, T. R.; Millevolte, A.; Gunsolus, I.; McGeachy, A.

- C.; Doğangün, M.; Li, T.; Hu, D.; Walter, S. R.; Mohaimani, A.; Schmoldt, A.; Torelli, M. D.; Hurley, K. R.; Dalluge, J.; Chong, G.; Feng, Z. V.; Haynes, C. L.; Hamers, R. J.; Pedersen, J. A.; Cui, Q.; Hernandez, R.; Klaper, R.; Orr, G.; Murphy, C. J.; Geiger, F. M. Lipid Corona Formation from Nanoparticle Interactions with Bilayers. *Chem* **2018**, *4* (11), 2709–2723.
- (76) Mandal, T.; Konduru, N. V.; Ramazani, A.; Molina, R. M.; Larson, R. G. Effect of Surface Charge and Hydrophobicity on Phospholipid-Nanoparticle Corona Formation: A Molecular Dynamics Simulation Study. *Colloid Interface Sci Commun* **2018**, *25*, 7–11.
- (77) Maity, A.; De, S. K.; Bagchi, D.; Lee, H.; Chakraborty, A. Mechanistic Pathway of Lipid Phase-Dependent Lipid Corona Formation on Phenylalanine-Functionalized Gold Nanoparticles: A Combined Experimental and Molecular Dynamics Simulation Study. *Journal of Physical Chemistry B* **2022**, *126* (11), 2241–2255.
- (78) Zhang, X.; Pandiakumar, A. K.; Hamers, R. J.; Murphy, C. J. Quantification of Lipid Corona Formation on Colloidal Nanoparticles from Lipid Vesicles. *Anal Chem* **2018**, *90* (24), 14387–14394.
- (79) Tahir, M. A.; Van Lehn, R. C.; Choi, S. H.; Alexander-Katz, A. Solvent-Exposed Lipid Tail Protrusions Depend on Lipid Membrane Composition and Curvature. *Biochimica et Biophysica Acta (BBA) Biomembranes* **2016**, *1858* (6), 1207–1215.
- (80) Moyano, D. F.; Saha, K.; Prakash, G.; Yan, B.; Kong, H.; Yazdani, M.; Rotello, V. M. Fabrication of Corona-Free Nanoparticles with Tunable Hydrophobicity. *ACS Nano* **2014**, *8* (7), 6748–6755.
- (81) Saha, K.; Moyano, D. F.; Rotello, V. M. Protein Coronas Suppress the Hemolytic Activity of Hydrophilic and Hydrophobic Nanoparticles. *Mater Horiz* **2013**, *1* (1), 102–105.
- (82) Van Lehn, R. C.; Alexander-Katz, A. Energy Landscape for the Insertion of Amphiphilic Nanoparticles into Lipid Membranes: A Computational Study. *PLoS One* **2019**, *14* (1), e0209492.
- (83) Van Der Spoel, D.; Lindahl, E.; Hess, B.; Groenhof, G.; Mark, A. E.; Berendsen, H. J. C. GROMACS: Fast, Flexible, and Free. *J Comput Chem* **2005**, *26* (16), 1701–1718.
- (84) Lindahl; Abraham; Hess; Spoel, van der. GROMACS 2021.5 Source Code. January 14, 2022.
- (85) Tribello, G. A.; Bonomi, M.; Branduardi, D.; Camilloni, C.; Bussi, G. PLUMED 2: New Feathers for an Old Bird. *Comput Phys Commun* **2014**, *185* (2), 604–613.
- (86) Marrink, S. J.; Risselada, H. J.; Yefimov, S.; Tieleman, D. P.; De Vries, A. H. The MARTINI Force Field: Coarse Grained Model for Biomolecular Simulations. *Journal of Physical Chemistry B* **2007**, *111* (27), 7812–7824.
- (87) De Jong, D. H.; Singh, G.; Bennett, W. F. D.; Arnarez, C.; Wassenaar, T. A.; Schäfer, L. V.; Periole, X.; Tieleman, D. P.; Marrink, S. J. Improved Parameters for the Martini Coarse-Grained Protein Force Field. *J Chem Theory Comput* **2013**, *9* (1), 687–697.
- (88) Yesylevskyy, S. O.; Schäfer, L. V.; Sengupta, D.; Marrink, S. J. Polarizable Water Model for the Coarse-Grained MARTINI Force Field. *PLoS Comput Biol* **2010**, *6* (6), e1000810.
- (89) Michalowsky, J.; Schäfer, L. V.; Holm, C.; Smiatek, J. A Refined Polarizable Water Model for the Coarse-Grained MARTINI Force Field with Long-Range Electrostatic Interactions. *Journal of Chemical Physics* **2017**, *146* (5), 54501.

- (90) Davis, R. S.; Sunil Kumar, P. B.; Sperotto, M. M.; Laradji, M. Predictions of Phase Separation in Three-Component Lipid Membranes by the MARTINI Force Field. *Journal of Physical Chemistry B* **2013**, *117* (15), 4072–4080.
- (91) Wassenaar, T. A.; Ingólfsson, H. I.; Böckmann, R. A.; Tieleman, D. P.; Marrink, S. J. Computational Lipidomics with Insane: A Versatile Tool for Generating Custom Membranes for Molecular Simulations. *J Chem Theory Comput* **2015**, *11* (5), 2144–2155.
- (92) Grunewald, F.; Rossi, G.; De Vries, A. H.; Marrink, S. J.; Monticelli, L. Transferable MARTINI Model of Poly(Ethylene Oxide). *Journal of Physical Chemistry B* **2018**, *122* (29), 7436–7449.
- (93) Ghose, A. K.; Crippen, G. M. Atomic Physicochemical Parameters for Three-Dimensional-Structure-Directed Quantitative Structure-Activity Relationships. 2. Modeling Dispersive and Hydrophobic Interactions. *J. Chem. Inf. Comput. Sci* **1987**, *27* (1), 21–35.
- (94) Hub, J. S.; De Groot, B. L.; Van Der Spoel, D. G-Whams-a Free Weighted Histogram Analysis Implementation Including Robust Error and Autocorrelation Estimates. *J Chem Theory Comput* **2010**, *6* (12), 3713–3720.